Time–frequency characterization of the unsteady phenomena in a centrifugal pump

G. Pavesi *, G. Cavazzini, G. Ardizzon

Department of Mechanical Engineering, University of Padova, Via Venezia 1, 35121 Padova, Italy

ARTICLE INFO

ABSTRACT

The paper presents an experimental investigation of the flow field instability in a centrifugal pump. Pressure fluctuations were measured with transducers placed flush with the inlet duct, and at the impeller discharge. Two impeller rotation speeds were utilized in the study, as well as several angular and radial transducer positions at design, and at off-design flow rates. A spectral analysis was carried out on the pressure signals in frequency and in time–frequency domains. The results highlighted the existence of an asymmetrical rotating pressure structure at the impeller discharge, having a fluid-dynamical origin and propagating both in the radial and circumferential direction, inside and downstream of the impeller.

© 2008 Elsevier Inc. All rights reserved.

1. Introduction

The unsteady phenomena which occur in a turbomachine and in particular those phenomena that are related to the rotor–stator interaction, negatively affect the machine's performance in terms of efficiency, vibrations, noises and pressure pulsations, especially at off-design conditions. In past years, several investigations have been carried out to study these phenomena, with some focusing on the noise generation mechanisms.

Cumpsty (1977) and Neise (1976) studied the tonal pulse generation in the centrifugal machines, demonstrating that changing the impeller and cut-off geometry could reduce the blade passage frequency tones. In 1963, Embleton (1963) implemented several design changes in the impeller and cut-off, such as sloping the cut-off and impeller blades, and including slots in the impeller blades.

Other techniques, based on the control of the spectral structure, were studied to reduce the level of the blade passage frequency noise. Neise and Koopmann (1980) used a resonator to remove the unsteady aerodynamics noise sources at the cut-off. Whereas, Koopmann et al. (1988) resorted to a dual-phased controlled loud speakers, placed at the cut-off. In 1994, Akin and Rockwell (1994) demonstrated that large and controlled perturbations at the inflow of a free impeller, as well as that of an impeller–diffuser system, can manipulate the spectral structure of the discharge and can significantly reduce the amplitude of the blade passage frequency (BPF) harmonics.

The noise spectral structure for studying the unsteady phenomena developing in the impeller passages and at the flow discharge

was also considered by researchers. Mongeau (Mongeau, 1991; Mongeau et al., 1993), Choi (Choi, 1991; Choi et al., 2003) and Bent (1993) identified a flow structure, having characteristics similar to the diffuser rotating stall, that was associated with the dominant unsteadiness of the spectrum at the impeller discharge. This structure rotated around the impeller at a fraction of the impeller's speed and, unlike the rotating stall, was characterized by a great number of azimuthal modes, which were found to comprise the stall.

The waterfalls signal presentation, based on the time–frequency analysis, was applied by Ferrara et al. (2004) for a more in-depth study of the rotating stall inception and evolution. Even the most advanced time–frequency analysis by means of wavelet was applied by a few researchers in the field of turbomachinery. For example, Horodko (2006, 2007) demonstrated the applicability of the wavelets to the turbomachinery field and characterized in the time–frequency domain the different phases of the surge development in the centrifugal compressors.

The objective of this research was to identify and characterize the unsteady phenomena produced in a centrifugal pump, utilizing the Fourier approach and the time–frequency analysis. A correlation between the fluid dynamics and the emitted noise was investigated in order not only to optimize the machine performance and to reduce the noise emission, but also to define the characteristic frequencies of the identified phenomena as a starting point for the definition of a non-intrusive diagnostic instrument.

2. Test facilities

The experimental analysis was performed in the Open Turbomachinery Facility (OTF), in the Department of Mechanical

---

Nomenclature

B	width [m]
C_m	meridional absolute velocity component [m/s]
d,e	integers [–]
D	diameter [m]
f	frequency [Hz]
g	gravitational constant [m/s^2]
$G^{xy}(f)$	cross-spectrum of signals x and y
h	pump head [m]
l	distance between the transducers [m]
n	time index of a signal
n_i	shaft speed [rpm]
N	number of signal segments (in Eq. (1)); number of signal samples (in Eq. (7)) [–]
n_b	number of blades [–]
$n_s = \frac{nQ^{0.5}}{h^{0.75}}$	specific speed [m$^{0.75}$s$^{-1.5}$]
Q	flow rate [m^3/s]
R	radius [m]
$R^2(s,n)$	wavelet coherence function [–]
$St = \frac{\pi D_2}{n_b}\frac{f}{U_2}$	Strouhal number based on the impeller tip speed [–]
U	peripheral velocity [m/s]
X	Fourier transform of the signal x
Y	Fourier transform of the signal y
$W(s,n)$	continuous wavelet transform
$W^{xy}(s,n)$	cross-wavelet spectrum
$WC^{xy}(s,\tau)$	wavelet cross-correlation function
W_H	weighting constant corresponding to the Hanning window [–]

β	relative flow angle [deg]
θ	angular position [deg]
$\gamma^2(f)$	coherence function [–]
γ_p	phase difference [deg]
$\varphi = \frac{C_{m2}}{U_2}$	flow coefficient [–]
$\phi(s,n)$	cross-wavelet phase difference [deg]
ω	angular rotation speed [s^{-1}]
$\omega_s = \omega\frac{Q^{0.5}}{(gh)^{0.75}}$	dimensionless specific speed [–]
τ	time delay [s]
$\psi(t)$	mother wavelet

Subscripts

1	rotor blade leading edge
2	rotor blade trailing edge
b	wavelet location
c	of the blade mean line
k	index
n	indication of a discrete-time signal
x,y	of the signals x and y
p	of the phenomenon
des	design
S	of the system
F	of the main pulsation frequency

Engineering, University of Padua. The OTF is a water test rig designed for testing the influence of several parameters on the overall performances of both pumps and turbines. The analyzed pump had an original configuration, constituted by a 3D impeller, coupled with a vaned diffuser and a vaned return channel, reproducing the first stage of a two-stage pump-turbine (ω_s = 0.71; n_s = 37.6 m$^{0.75}$s$^{-1.5}$) (Ardizzon and Pavesi, 2004). To remove the noise sources due to stator–rotor interaction, the pump configuration was modified to operate with an axially symmetric vaneless diffuser. Table 1 reports the diameter (D_2), the width (B_2), the blades number (n_b) and the blade angle (β_{2c}) of the tested pump, as well as the flow coefficient at design point (φ_{des}).

Measurements of the unsteady pressure were carried out at different radial and angular positions.

Fig. 1 shows a schematic view of the tested configuration with the reference marks of the measurement positions:

- three positions, 68 mm upstream the impeller, in the inlet duct (positions 10, 11 and 12 – white marks in Fig. 1);
- four positions, 2 mm downstream the impeller (positions 20, 21, 22 and 23 – dark gray marks in Fig. 1);
- two positions, 26 mm downstream the impeller (positions 30 and 31 – light gray marks in Fig. 1).

Pressure transducers, placed flush with the wall, acquired unsteady pressure signals. Two piezoresistive transducers suited for dynamic and static pressure measurements (sensitivity of about

29 mV bar^{-1}) and a piezoelectric dynamic pressure transducer (sensitivity of 7.3e$-$3 V kPa^{-1}) were circumferentially equidistant in the inlet duct (positions 10, 11 and 12); three piezoresistive transducers (sensitivity of about 29 mV bar^{-1}), equidistant around the circumference, and a piezoelectric transducer (sensitivity of 7.3e$-$3 V kPa^{-1}) were located 2 mm downstream the impeller (positions 20, 21, 22 and 23), whereas two piezoresistive transduc-
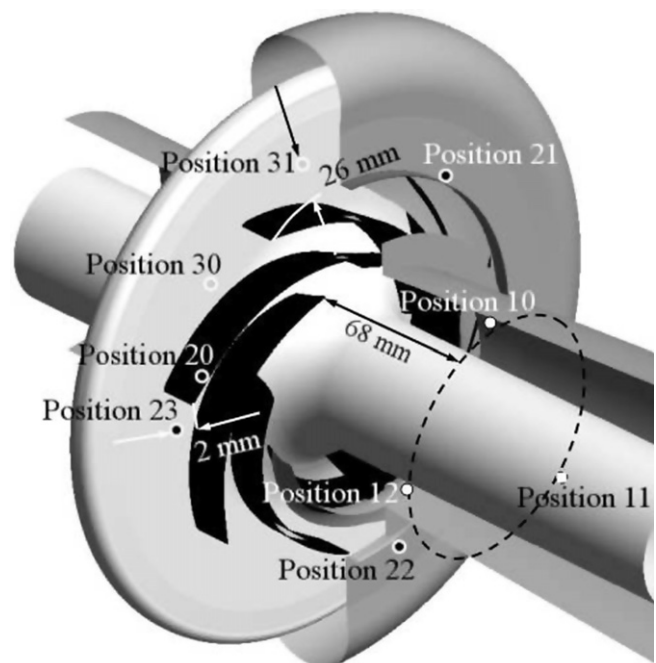
Table 1
Impeller data

D_2 (mm)	B_2 (mm)	n_b	β_{2c}	φ_{des}
400	40	7	26.5	0.125

Fig. 1. Schematic view of the tested configuration.

Table 2
Analyzed operating conditions

Q/Q_{des} (%)	Q (m^3 s^{-1})	φ	$\delta Q/Q$	n_i (rpm)	
20	0.016	0.025	0.112		
40	0.032	0.050	0.027		
50	0.040	0.063	0.018		
60	0.048	0.075	0.014	500	600
80	0.063	0.100	0.011		
100	0.079	0.125	0.010		
120	0.095	0.150	0.009		

ers (sensitivity of about 29 mV bar^{-1}) were placed 26 mm downstream the impeller with an angular distance of about 49° (positions 30 and 31). The sensors' combined non-linearity, hysteresis and repeatability was better than 0.1%. The data were simultaneously acquired from all the channels at a sampling rate of 2048 Hz and recorded by a workstation controlled transient data recorder, with a dynamic range of 24-bit. The outputs from the transducer channels were conditioned with a low-pass filter at 1024 Hz cut-off frequency.

Seven different operating conditions, reported in Table 2 with the relative accuracy $\delta Q/Q$, and two impeller rotation speed (n_i = 500 rpm; 600 rpm) were investigated.

3. Signal processing

The pressure signals were analyzed both in the frequency domain and in the time–frequency domains.

Auto-spectral and cross-spectral matrices were computed by partitioning each time signal into 256 non-overlapping segments of 2^{12} samples, filtered with a Hanning window for avoiding leakage errors. The frequency resolution was 0.5 Hz. The auto-spectra and the cross-spectra were determined from the following equation:

$$G^{xy}(f) = \frac{1}{NW_H} \sum_{k=1}^{N} [X_k^*(f)Y_k(f)] \tag{1}$$

where N is the number of segments (i.e. $N = 256$), W_H is weighting constant corresponding to the Hanning window, $Y_k(f)$ is the fast Fourier transform of the kth data segment of the signal y and $X_k^*(f)$ is the complex conjugate of the fast Fourier transform of the kth data segment of the signal x. The number of the time segments ($N = 256$) was established, as twice the lowest values whose increase did not involve a significant variation in the resulting function $G^{xy}(f)$.

For a better presentation of the results, the power spectra and the cross-spectra were sometimes displayed in a decibel scale, where the decibel is defined as

$$dB = 10\log_{10} G^{xy}(f) \tag{2}$$

The coherence function $\gamma^2(f)$:

$$\gamma^2(f) = \frac{|G^{xy}(f)|^2}{G^{xx}(f)G^{yy}(f)} \tag{3}$$

between two signals was also considered. The square cross-spectrum $G^{xy}(f)$ was divided by the product of the signal auto-spectra ($G^{xx}(f), G^{yy}(f)$) to measure the degree of linearity between the two signals versus the frequency in the normalized range from 0 to 1.

The phase information, obtained by the cross-correlation analysis between transducers placed at the same radial distance and at different angular positions (Eq. (1)), allowed to identify the existence of coherent structures and to calculate their rotation velocity. However, since the phase values are always included between −180° and +180°, a phase difference between two signals greater

than one period results to be lower than one period anyway. So, in order to correctly evaluate the phase difference, the adjacent frequencies were analyzed and the previous periods were considered in the global calculation of the phase (Choi, 1991; Mongeau, 1991; Bent, 1993).

Having the phase difference γ_p for the frequency f, the time delay τ corresponding to that frequency was calculated as

$$\tau = \frac{\gamma_p}{360 f} \tag{4}$$

The angular rotation velocity ω_p of the identified structure, normalized by the angular impeller rotation speed ω, can be determined by the following equation:

$$\frac{\omega_p}{\omega} = \frac{\Delta\theta}{\tau} \frac{60}{2\pi n_i} = \frac{f\Delta\theta}{\gamma_p} 60 \frac{360}{2\pi n_i} \tag{5}$$

when the time delay τ, the angular distance between the transducers $\Delta\theta$ and the impeller rotational speed n_i are known.

In order to evaluate the propagation velocity C_p of the identified structure downstream of the impeller, Eq. (5) was adapted for transducers placed at different radial and azimuthal positions:

$$\frac{C_p}{U_2} = \frac{l}{\tau} \frac{60}{2\pi n_i} \frac{1}{R_2} = \frac{fl}{\gamma_p} 60 \frac{360}{2\pi n_i} \frac{1}{R_2} \tag{6}$$

where R_2 and U_2 are, respectively, the radius and the peripheral velocity at the impeller blade trailing edge, and l is the distance between the transducers.

The signal processing in the frequency domain allows finding and analyzing the spectral components contained in the measured pressure signals, but it does not allow an assignment of these spectral components to time. In order to provide information about their time evolution, a time–frequency analysis was carried out by means of the wavelet transforms.

The continuous wavelet transform $W(s,n)$ of the discrete sampled pressure signal x_n was computed via the FFT-based fast convolution:

$$W(s,n) = \sum_{k=0}^{N-1} X_k \left(\sqrt{\frac{2\pi s}{\delta t}} \Psi_0^*(s\omega_k) e^{i\omega_k n\delta t} \right) \tag{7}$$

where X_k is the discrete Fourier transform (DFT) of x_n, k is the frequency index, N is the data series length, s is the wavelet scale, δt is the sampling interval, n is the localized time index, $\Psi_0^*(s\omega_k)$ is the complex conjugate of the Fourier transform of the scaled version of the "mother wavelet" $\psi(t)$, ω_k is the angular frequency (if $k \leqslant N/2$, $\omega_k = 2\pi k/N\delta t$; else $\omega_k = -2\pi k/N\delta t$). The equation contains a normalization factor $\sqrt{2\pi s/\delta t}$ to obtain unit energy at each scale. The choice of the best mother wavelet depends on several factors (Farge, 1992). In this paper the complex Morlet wavelet (with $2\pi f_0 = 6$) was chosen, since it provided a good balance between time and frequency localization and it returned information about both amplitude and phase.

In order to determine the relation between two pressure signals $x(t)$ and $y(t)$ in the time–frequency domains, the wavelet cross-correlation function, defined by Li (1998), was introduced:

$$WC^{xy}(s,\tau) = \lim_{T\to\infty} 1/T \int_{-T/2}^{T/2} W^{x*}(s,b)W^y(s,b+\tau)db \tag{8}$$

where τ is the time delay between the two signals, W^y is the continuous wavelet transform of $y(t)$, W^{x*} is the complex conjugate of the continuous wavelet transform of $x(t)$, b is the position and s is the scale.

Additionally, for two sampled pressure signals x_n and y_n with wavelet transforms $W^x(s,n)$ and $W^y(s,n)$, the cross-wavelet spectrum was determined as

$$W^{xy}(s,n) = W^x(s,n)W^{y*}(s,n) \tag{9}$$

where $W^{y*}(s,n)$ is the complex conjugate of $W^y(s,n)$ (Torrence and Compo, 1998).

Finally the wavelet coherence function, measuring the coherence between two sampled signals x_n and y_n both in frequency bands and in time intervals, was considered:

$$R^2(s,n) = \frac{|\langle W^{xy}(s,n)\rangle|^2}{\langle |W^y(s,n)|^2\rangle \langle |W^y(s,n)|^2\rangle} \tag{10}$$

where $\langle \cdots \rangle$ indicates a smoothing, done using a weighted running convolution in both the time and scale directions, that depends on the mother wavelet (Torrence and Compo, 1998; Torrence and Webster, 1999). For the complex Morlet wavelet function, the time smoothing was done using the absolute value of the wavelet function at each scale, normalized to have a total weight of unity, with a Gaussian $\exp(-t^2/(2s^2))$. The scale smoothing was done using a boxcar filter of width δj_0. The smoothing scale factor δj_0 is empirically determined for each mother wavelet: for the Morlet wavelet is equal to 0.60 (Torrence and Compo, 1998; Torrence and Webster, 1999). In the numerator, the real and imaginary parts of the cross-wavelet spectrum were smoothed before the absolute value was calculated, whereas in the denominator the smoothing was done on the square wavelet power spectra of the two signals.

The smoothed real (Re) and imaginary (Im) parts of the wavelet cross-spectrum were used for determining the phase difference:

$$\phi(s,n) = \tan^{-1}\left(\frac{\mathrm{Im}(\langle W^{xy}(s,n)\rangle)}{\mathrm{Re}(\langle W^{xy}(s,n)\rangle)}\right) \tag{11}$$

4. Results

4.1. Analysis of the pressure signals

Stator–rotor interaction causes a pronounced pressure pulsation system.

Figs. 2 and 3 report the power spectra [dB] of the unsteady pressure, measured in the inlet duct (position 10) and at 2 mm downstream the impeller discharge (position 20) versus the Strouhal number (St), a non-dimensional frequency based on the circumferential blade-to-blade distance and the impeller tip speed.

In these measurement positions, as well as for all the others (positions 11–12; 21–23), with the exception of blade passage frequency (BPF) and its harmonics, both the spectra were dominated by two peaks: the main one at $St_F = 0.664$ and the second one at $St_S = 0.071$. All other peaks in the spectra were harmonics of these fluctuations or non-linear components, generated by the interaction between the first pressure pulsations' frequency (at $St_F = 0.664$) and the BPF:

$$dSt_F \pm eSt_{BPF}$$
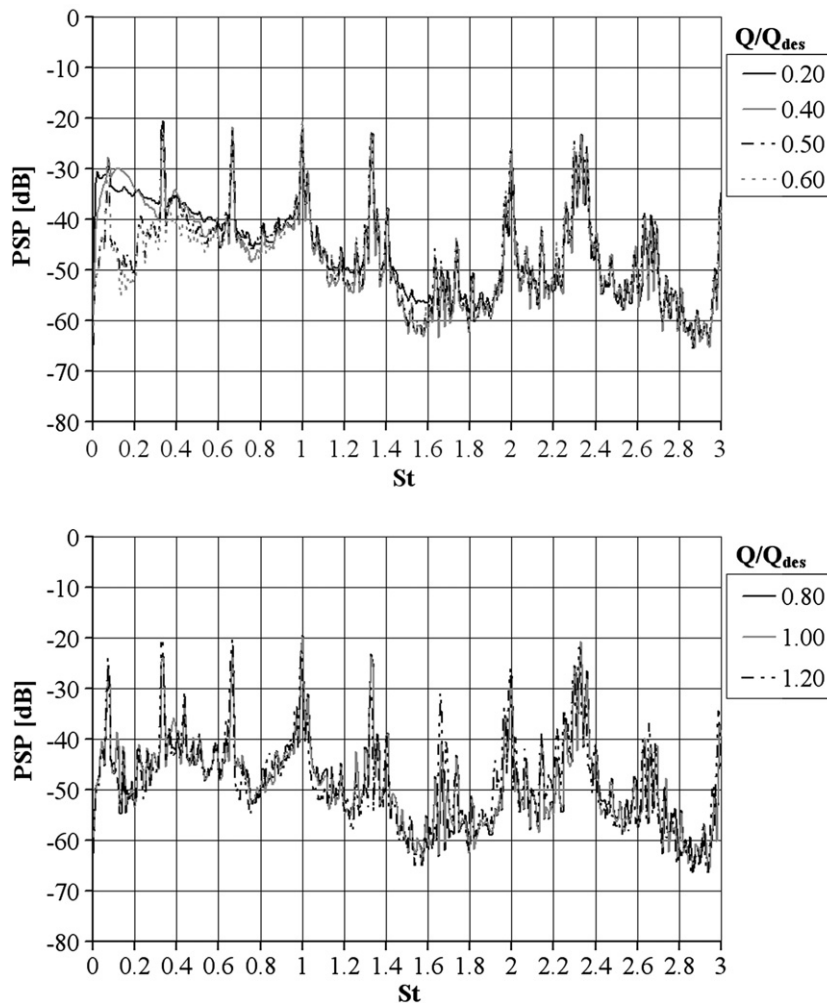$$(d, e = \text{integer}) \tag{12}$$

Fig. 2. Power spectrum [dB] of the pressure measured in the inlet duct (position 10) (n_i = 600 rpm).
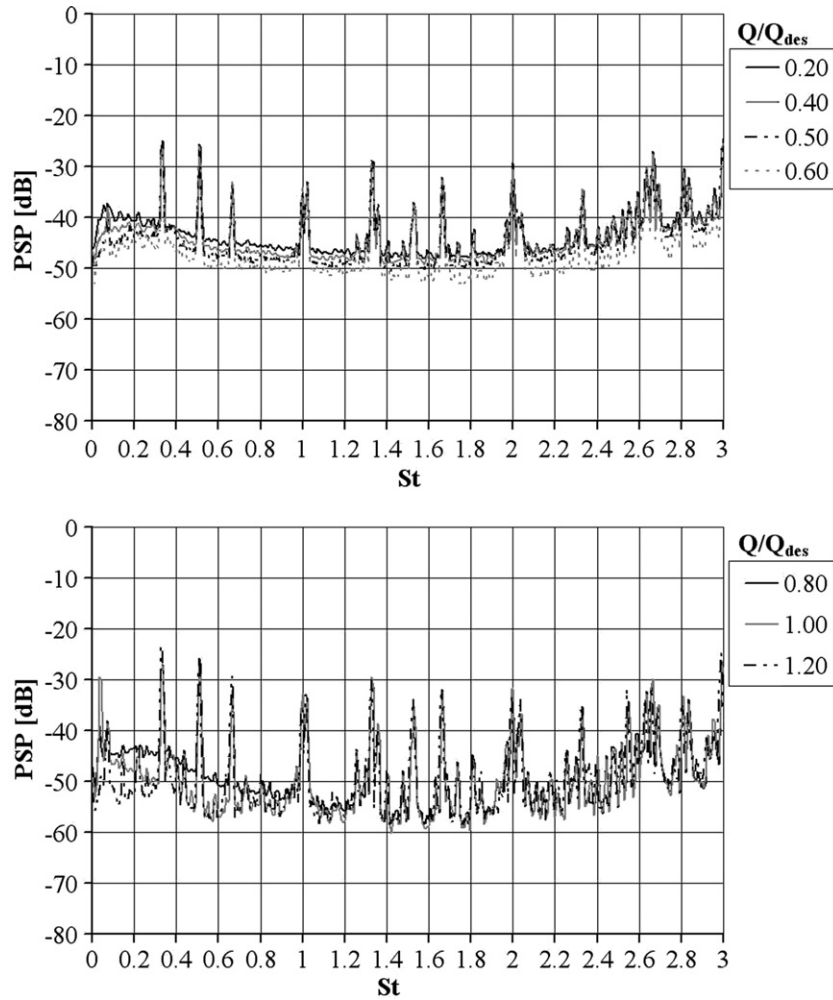
Fig. 3. Power spectrum [dB] of the pressure measured at the impeller discharge (position 20) (n_i = 600 rpm).

or between the pressure pulsations frequency at St_F = 0.664 and the other pulsations frequency at St_S = 0.071:

$$dSt_F \pm eSt_S \tag{13}$$
$$(d, e = \text{integer})$$

Table 3 reports some identified non-linear interaction components.

The pressure pulsation at St_S = 0.071, corresponding to a frequency of 5 Hz, was identified with the impeller not running (Fig. 4). For this reason it appears to be associated with system fluctuations and in particular with the fluctuation of the water level in the accumulation tank of the pump. With a greater intensity of the phenomenon observed in the inlet duct and the time-independent behaviour for all the flow rates (Figs. 5 and 6), the time–frequency analysis supports this hypothesis.

Figs. 5 and 6 report the continuous wavelet transform of the pressure signals acquired in the impeller inlet (position 10) and outlet (position 20), respectively, for Q/Q_{des} = 100% and for Q/Q_{des} = 60%. The wavelet magnitude at St_S = 0.071, in the inlet duct,
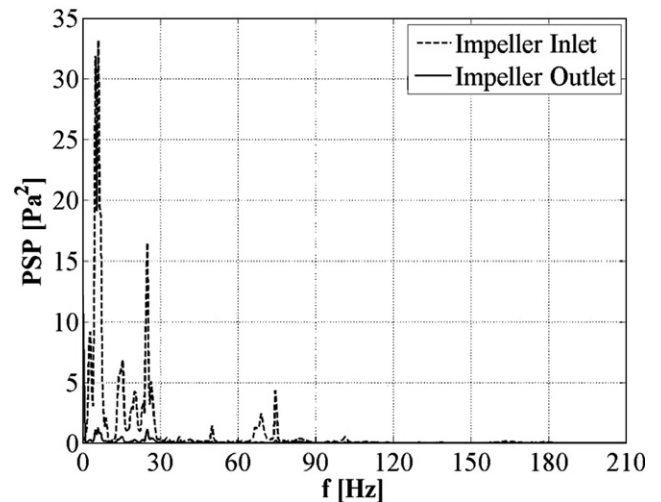

Fig. 4. Power spectrum [Pa²] of the pressure measured in positions 10 and 20 with the pump not running.

Table 3
Some identified non-linear interaction components

St	Non-linear components	St	Non-linear components
0.164	$St_F - 7St_S$	1.021	$St_F + 5St_S$
0.336	$St_{BPF} - St_F$	1.164	$St_F + 7St_S$
0.521	$St_F - 2St_S$	1.185	$2St_F - 2St_S$
0.736	$St_F + St_S$	1.664	$St_F + St_{BPF}$
0.807	$St_F + 2St_S$	2.300	$4St_F - 5St_S$
0.971	$2St_F - 5St_S$	2.328	$St_{BPF} + 2St_F$
1.014	$5St_{BPF} - 6St_F$	2.664	$2St_{BPF} + St_F$

was characterized by a constant value for the whole time interval, whose intensity decreased noticeably at the impeller discharge (Figs. 5 and 6).

The wavelet transformation at other flow rates showed similar results, with the peak amplitude at $St_S = 0.071$, which increased with the flow rate (Fig. 7).

This result appears to reconfirm the hypothesis of a dependence of the pressure pulsation St_S on system noise. Since, the water supplied by the service caused a water level fluctuation in the accumulation tank that greatly increased with the flow rate.

At $St_S = 0.071$ the coherence level between the signals, acquired at the impeller inlet (position 10) and outlet (position 20), reached values greater than 0.6 (Fig. 8). The notable coherence in the time–frequency domain was confirmed by the high values of the wavelet coherence, reported in Fig. 9 for $Q/Q_{des} = 100\%$. In this figure, as in all the following figures regarding the cross-wavelet and the wavelet coherence, the arrows represent the phase difference between both the signals considered. The in-phase relation was presented as arrows pointing right, the anti-phase relation as arrows pointing left, the 90° phase offset as arrows pointing straight on.

The pressure pulsation at $St_F = 0.664$ had a fluid-dynamical origin, due to the absence of this frequency in the spectra of the not-running pump (Fig. 4).
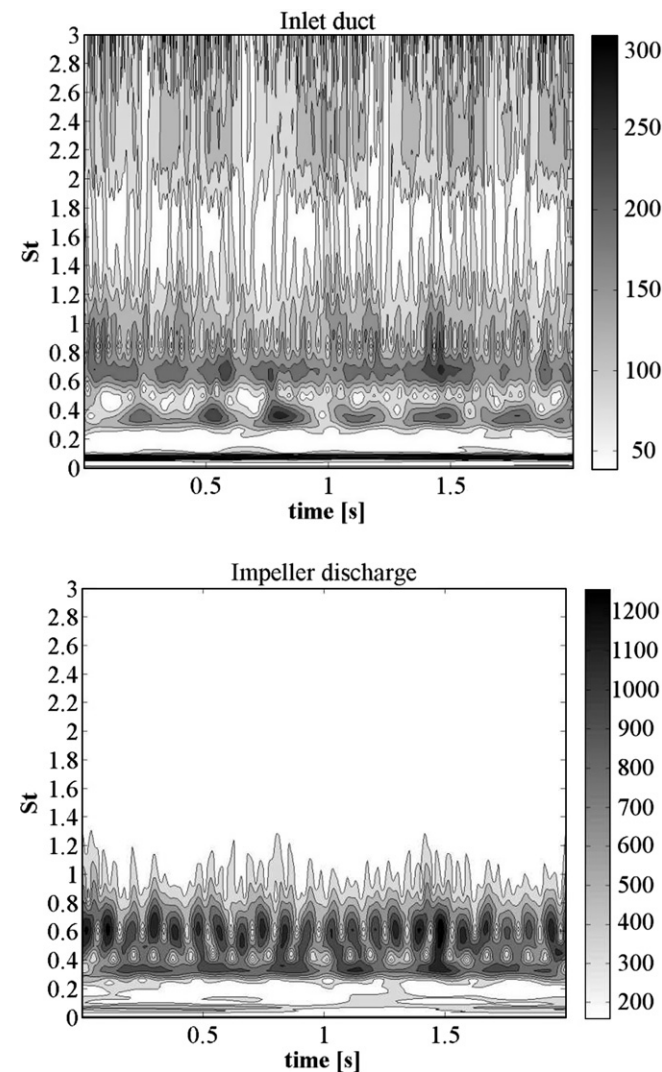

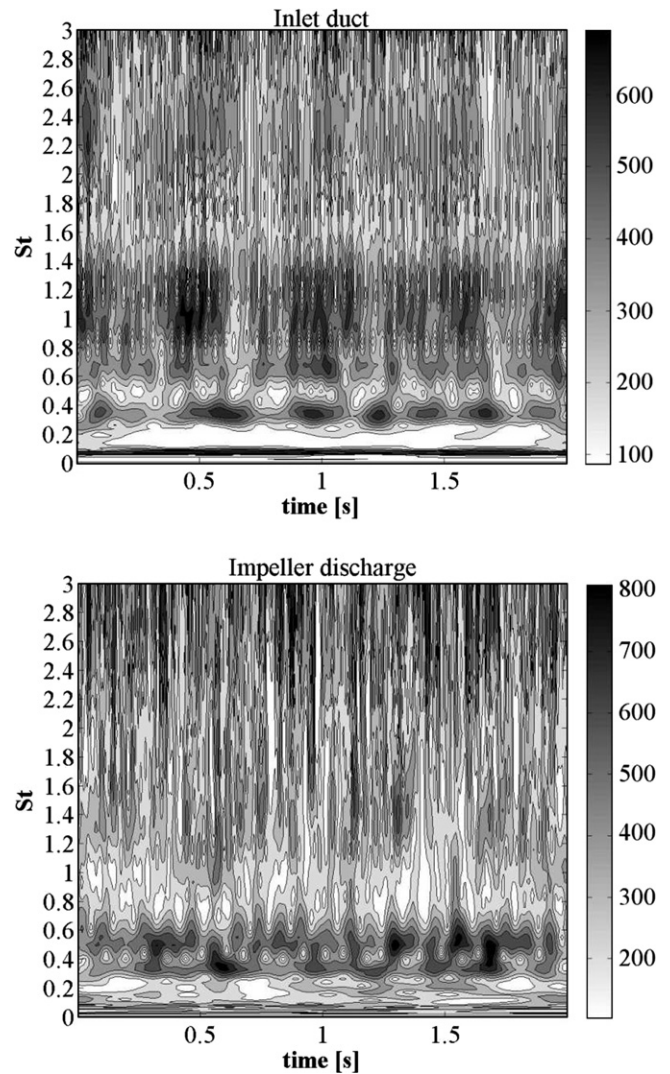**Fig. 5.** Wavelet transform magnitude |W| [Pa] in positions 10 and 20 for $Q/Q_{des} = 100\%$.

Fig. 6. Wavelet transform magnitude |W| [Pa] in positions 10 and 20 for $Q/Q_{des} = 60\%$.

As demonstrated by Akin and Rockwell (1994), an unsteady forced perturbation of the fluid flow in a pump, generates non-linear interaction components in the power spectra. The existence of several non-linear interaction components associated with the fundamental frequency at $St_F = 0.664$, appears to identify this unsteady perturbation to a non-forced fluid-dynamical unsteadiness, as it was not identified with the pump not running.

The existence of this fluid-dynamical unsteadiness was also confirmed by the time–frequency analysis at all the flow rates. As seen in Fig. 5, for $Q/Q_{des} = 100\%$, the wavelet transforms were characterized by greater values for the frequency at $St_F = 0.664$. Moreover, at this frequency the wavelet magnitude was not constant in the time domain, but it had a pulsating behaviour. This pulsation had a great regularity at the impeller discharge that decreased with decreasing flow rate (Figs. 5 and 6).

The pulsating behaviour also characterized the non-linear interaction component at $St = 0.336$, having great wavelet magnitude, and some other non-linear components with high frequencies and with lower wavelet transform magnitude (Figs. 5 and 6). As expected, their pulsation was very similar to the pulsation at $St = 0.664$, as they were the result of the interaction between the pulsating unsteady pattern at $St = 0.664$ and the BPF, always present in time.
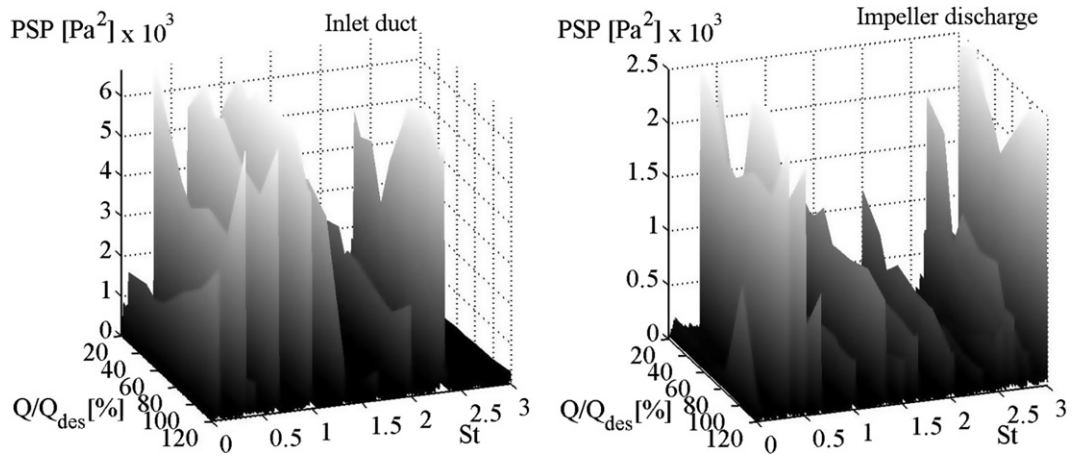
Fig. 7. Power spectrum [Pa^2] of pressure measured in positions 10 and 20 as a function of the flow rate (n_i = 600 rpm).
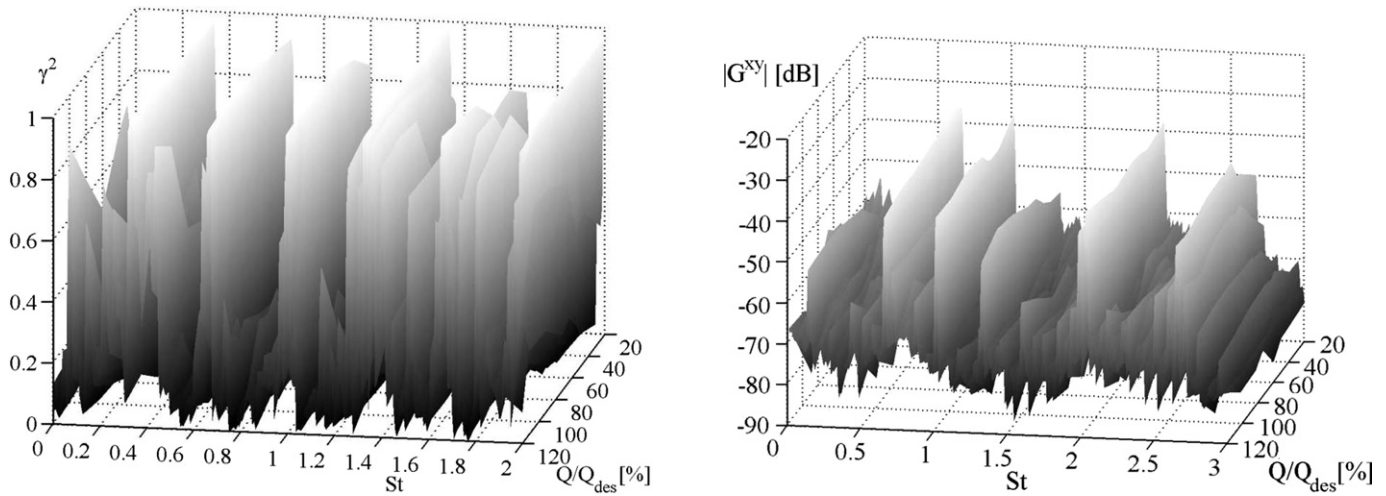

Fig. 8. Coherence level between inlet (position 10) and impeller discharge (position 20) (n_i = 600 rpm).
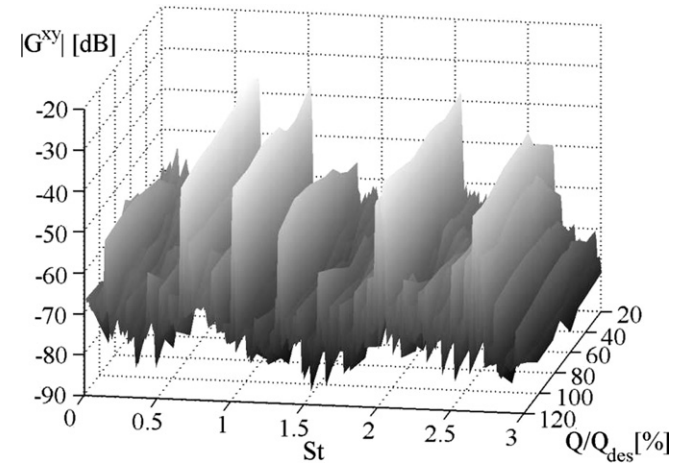

Fig. 10. Modulus of the cross-spectrum [dB] between the pressure transducers in positions 21 and 22 (n_i = 600 rpm).
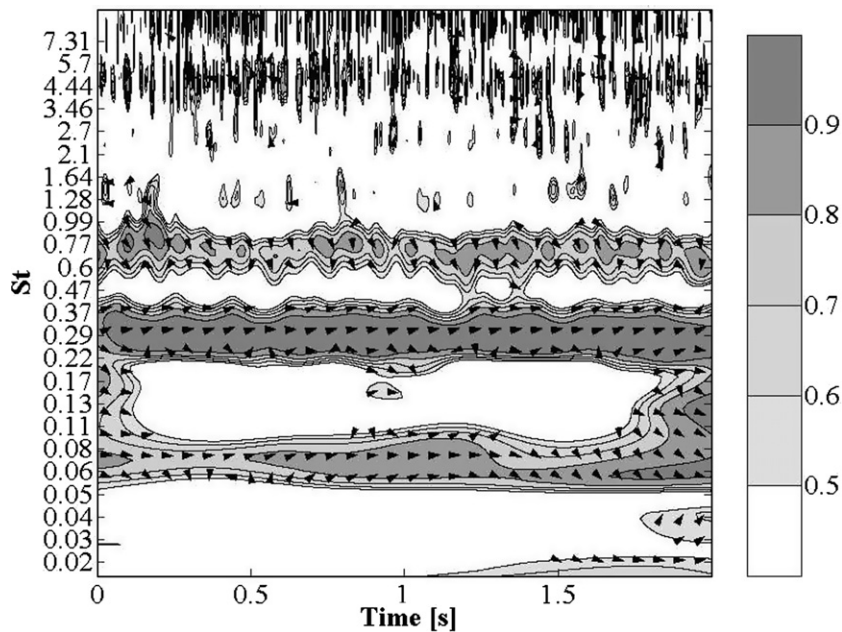

Fig. 9. Wavelet coherence between inlet (position 10) and impeller discharge (position 20) for Q/Q_{des} = 100% (n_i = 600 rpm).
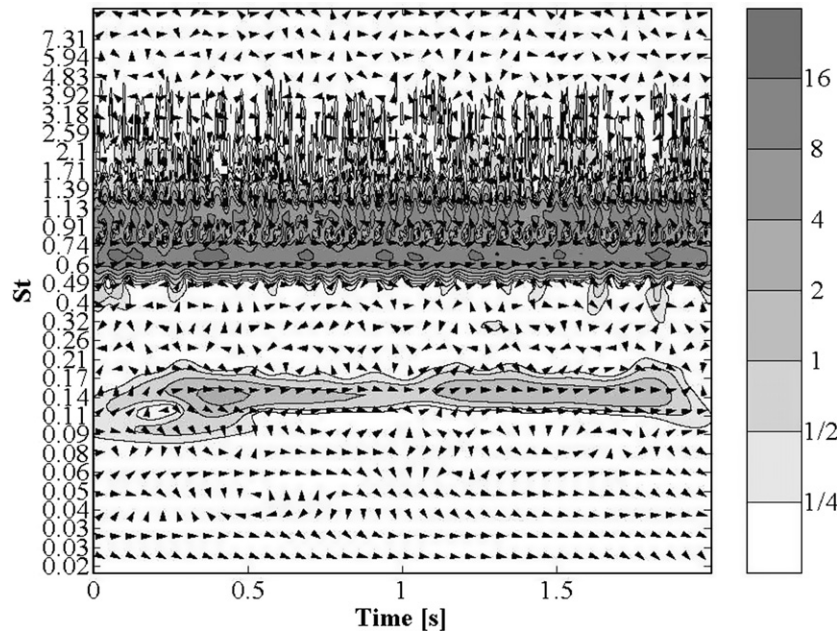
Fig. 11. Cross-wavelet transform between the pressure transducers in positions 21 and 22 for Q/Q_{des} = 120% (n_i = 600 rpm).
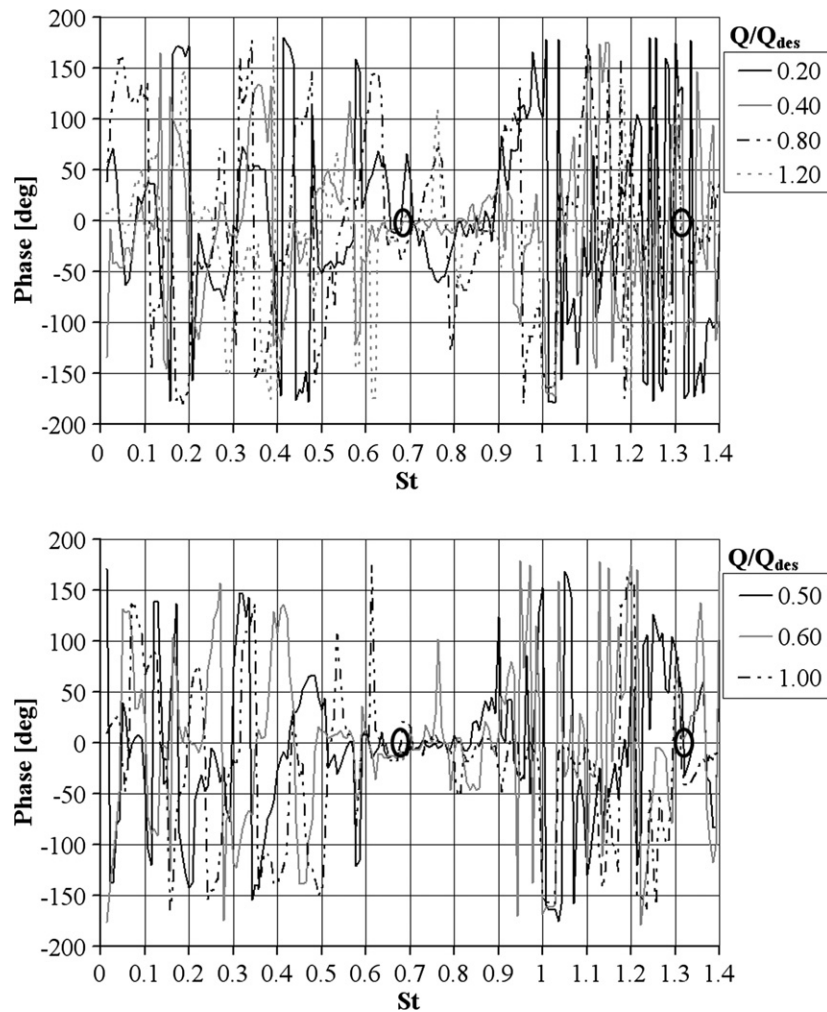

Fig. 12. Phase of the cross-spectrum between the pressure transducers in positions 21 and 22 (n_i = 600 rpm).

It seemed that all these modes, constituting the fluid-dynamical unsteadiness, interfered with one another alternately in a constructive and destructive way. So the resulting structure was not frozen in time, but it changed with a pulsating behaviour, appearing and disappearing, depending on the interference of its modes.

The presence of the BPF was not always well defined, as its magnitude was often less than that of the other frequencies (Figs. 5 and 6). A possible explanation for the low BPF amplitude could be the existence of the unsteady pattern that determined a "natural" manipulation of the spectrum components, redistributing the BPF energy among the harmonics and the non-linear interaction components and hence lowering the BPF intensity (Akin and Rockwell, 1994). Moreover, when the BPF was identifiable, it appeared to be pulsating as well as the frequencies of the unsteady pattern. This apparent pulsating behaviour could be explained by the proximity of three non-linear interaction components ($St = 0.972$, 1.014, 1.021) collectively with the limited resolution in the frequency domain of the wavelet transform, due to the Heisenberg uncertainty.

The characteristic frequencies of the unsteady pattern did not seem to be affected by the flow rate (Figs. 2 and 3), whereas the amplitude of its peaks presented higher values at low and high flow rates (Fig. 7).

The frequency of the unsteady pattern ($St_F = 0.664$), as well as several of its non-linear interaction components, had high cross-spectrum values and coherence levels greater than 0.6 for all the flow rates (Fig. 8). Moreover, the fundamental frequency ($St_F = 0.664$) reached high values of the cross-wavelet and the wavelet coherence in the entire analyzed time interval for all the flow rates (Fig. 9 for $Q/Q_{des} = 100\%$). Thus, confirming a continuous propagation of the pressure pulsations of the unsteady pattern inside the impeller.

4.2. Propagation in the circumferential direction of the identified unsteady structure

Pressure signals acquired at the impeller discharge at the same radial distance, but at different angular positions were compared for evaluating the stationary or rotating characteristics of the identified unsteady pattern. The comparison between the pressure transducers, placed 2 mm downstream the impeller (positions 20, 21, 22 and 23), highlighted high levels of the cross-spectrum and coherence functions in both frequency and time–frequency domains. Propagation of the phenomenon in the circumferential direction in the entire working range of the pump was also seen. Fig. 10 reports the cross-spectrum between the transducers placed in the positions 21 and 22, as a function of the flow rate, whereas Fig. 11 shows the cross-wavelet transform between the same transducers for $Q/Q_{des} = 120\%$. The cross-wavelet transform showed that the correlation in the circumferential direction did not seem to be a function of time (Fig. 11).
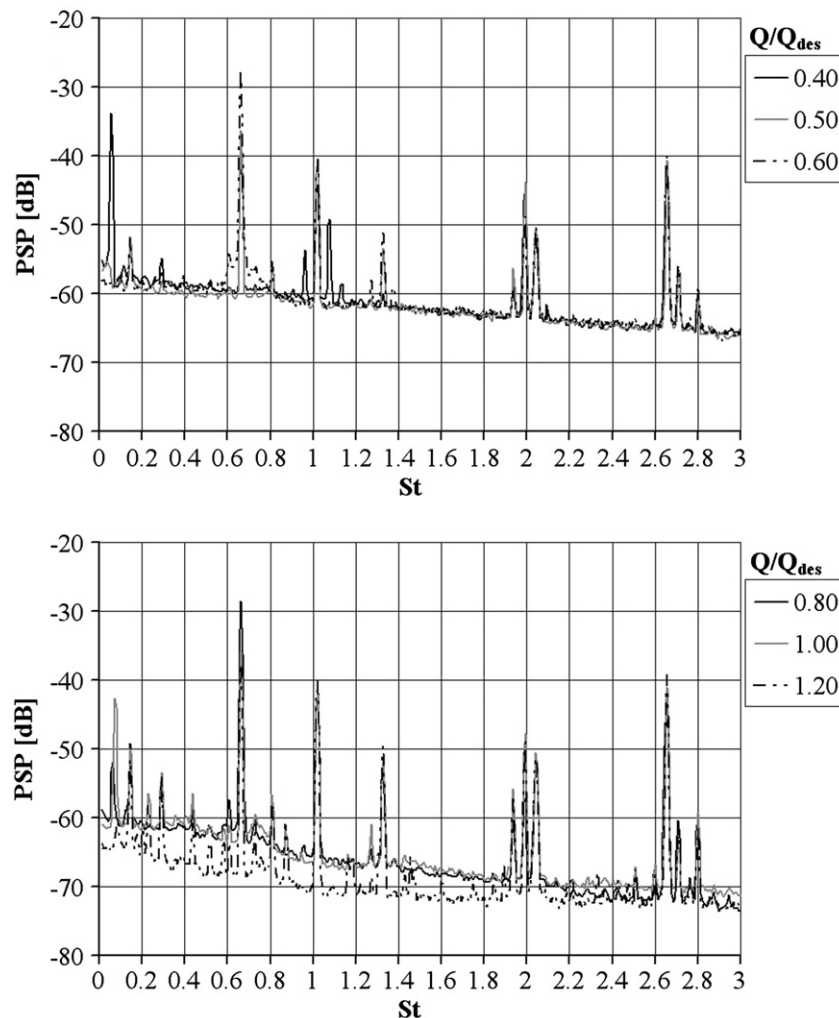

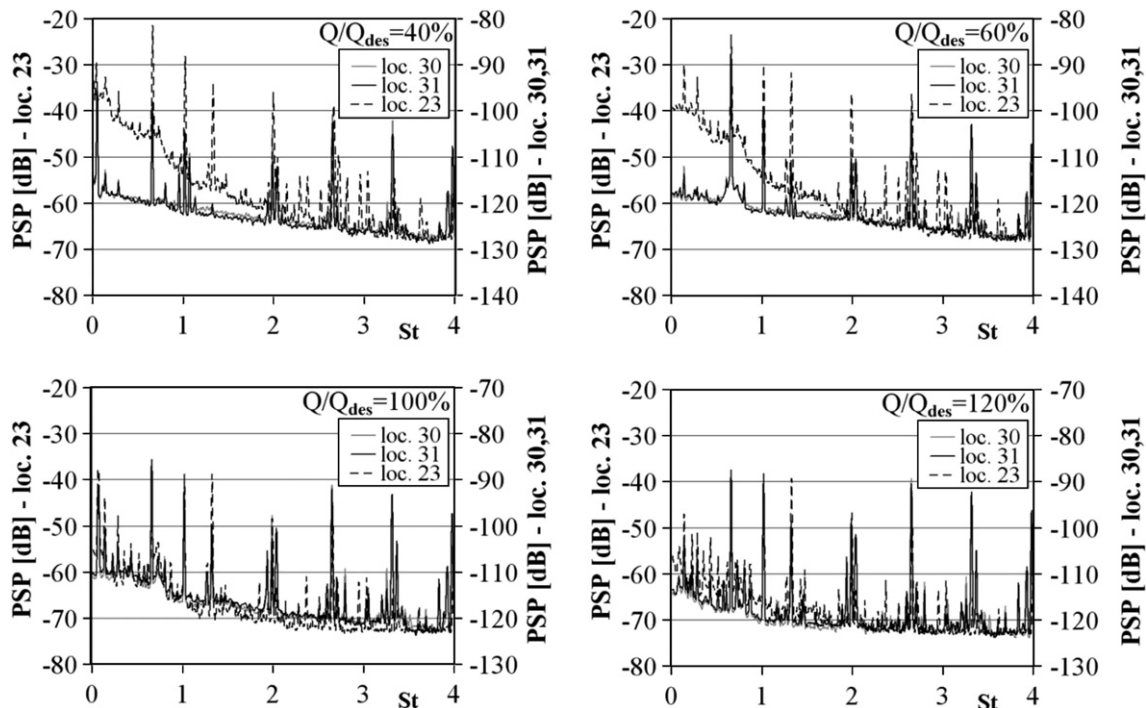**Fig. 13.** Power spectrum [dB] of the pressure signal acquired in position 30 ($n_i = 600$ rpm).

Fig. 14. Comparison of the power spectra [dB] of pressure signals acquired 2 mm (position 23) and 26 mm downstream the impeller (positions 30 and 31) ($n_i = 600$ rpm).

All these results proved the existence of a well-organized unsteady pattern, continuously involving the discharge of the impeller, whose modes interfered in a constructive and destructive way, determining the pulsating characteristics seen in Figs. 5 and 6. With regards to the phase difference, Fig. 11 highlights a time-independent phase coincidence (arrows pointing right) of the fundamental frequency of the pattern ($St = 0.664$), confirmed by the analysis of the phase of the cross-spectra (Fig. 12).

Known as the phase difference γ_p, the angular rotation speed ω_p of the unsteady pattern was determined with Eq. (5). The pressure instability speed was found to be 31.5% of the impeller rotation velocity. The same result was obtained with the cross-spectra between the other transducer signals.

4.3. Propagation in the radial direction of the identified unsteady structure

At a greater radial distance from the impeller discharge, the unsteady pattern did not change its characteristics and configuration. The spectral structure of the pressure signals, acquired 26 mm downstream the impeller (positions 30 and 31), was not different from that acquired immediately at the impeller discharge (positions 20–23). The unsteady pattern frequencies were still identifiable, whereas some non-linear interaction components disappeared at low flow rates (Fig. 13). The majority of these components were generated by the interaction between the unsteady pattern and the water level fluctuations in the accumulation tank. Their disappearance could be explained by the low intensity of the system fluctuations at low flow rates, which resulted in a quick damping of the associated non-linear components in the radial direction. At high flow rates, when the intensity of the system fluctuations was greater, they remained identifiable 26 mm downstream the impeller.

The comparison between the spectra of the transducers at different radial positions highlighted another aspect. The broadband level of the power spectrum of the transducer closer to the impeller blades (positions 20–23) was higher than those of the other two more distant transducers (positions 30 and 31) (Fig. 14). The differences of the power level were greater at low flow rates and diminished increasing the flow rate up to the design conditions. At higher flow rates, these differences started to increase again. This behaviour was associated with the wakes from the impeller blades. At low flow rates, the turbulence close to the impeller discharge, associated with these wakes, was intense. Proceeding in the radial direction, the wakes rapidly mixed with the mean flow coming out from the impeller, decreasing the turbulence level and associated noise. As the flow rate increased, the turbulence of the wakes diminished up to the design operating conditions, whereas at higher flow rates it started again to increase.

The hypothesis of a transmission of the pressure pulsations of the unsteady pattern in the radial direction, suggested by the comparison of the spectral contents, was confirmed by the cross-anal-
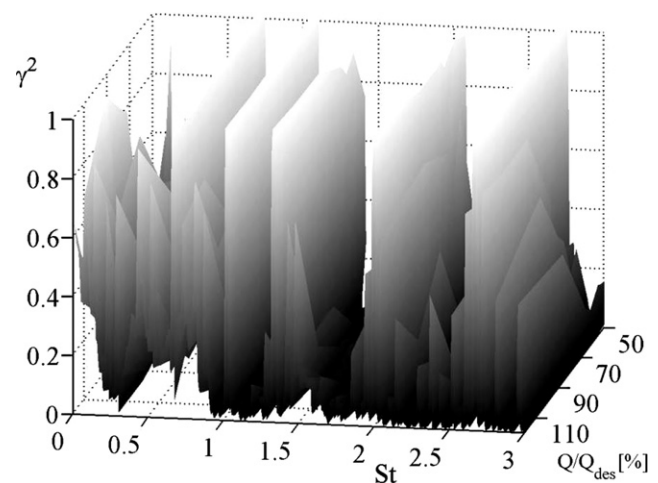

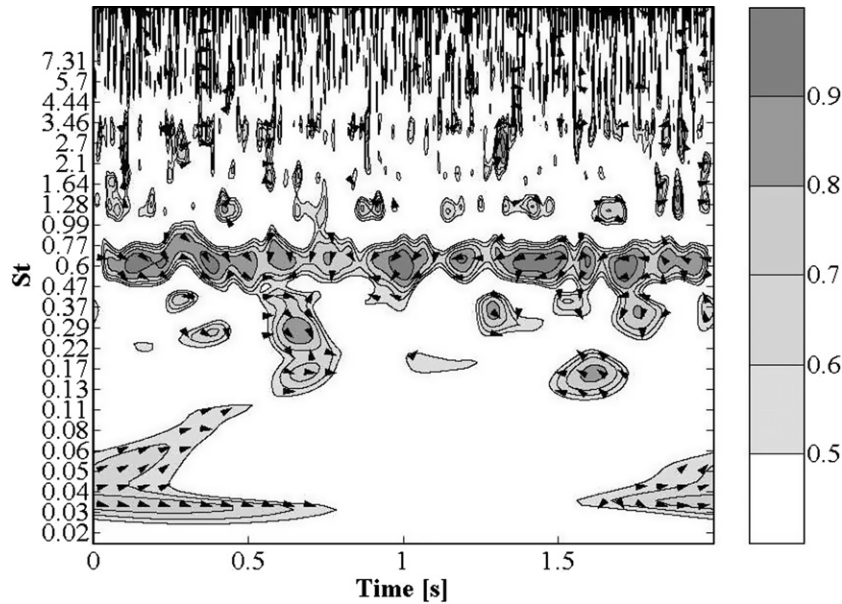**Fig. 15.** Coherence function between the pressure transducers in positions 20 and 30 ($n_i = 600$ rpm).

Fig. 16. Wavelet coherence between the pressure transducers in positions 20 and 30 for Q/Q_{des} = 40% (n_i = 600 rpm).

ysis between the signals of the transducers placed at the different radial positions, i.e. 2 mm and 26 mm downstream the impeller. Throughout the working range, the frequencies of the phenomenon were characterized by high values of the cross-spectrum and coherence functions in both the frequency and the time–frequency domains, as seen in Figs. 15 and 16 (for Q/Q_{des} = 40%). Since the transducers were placed at different radial and angular positions, the propagation velocity of the unsteady structure between them was determined by the Eq. (6) and it was found to variate from 34.3% to 35.0% of the peripheral velocity at the impeller blade trailing edge, depending on the flow rate. So, the propagation velocity in the radial direction resulted to be between 8.2% and 11.6% of the impeller peripheral velocity U_2, and to increase with the flow rates.

This propagation in the radial direction modified neither the pulsating characteristics of the unsteady pattern, as shown in Fig. 17 for Q/Q_{des} = 120%, nor its rotating movement in the circumferential direction. The harmonics of the phenomenon, as well as some of its non-linear interaction components, were characterized

by greater values of the cross-spectrum and of the coherence function (Fig. 18) between the transducers placed in positions 30 and 31 (26 mm downstream the impeller with an angular distance of 49°).

In the time–frequency domain, the cross-wavelet function and the wavelet coherence function were also characterized by greater values at some harmonics of the pattern, as shown in Fig. 19 for Q/Q_{des} = 50%. Moreover, at these frequencies both time–frequency functions highlighted a phase coincidence that confirmed the preservation of the unsteady pattern rotation in the circumferential direction and at a greater radial distance from the impeller discharge. The rotation velocity, determined from the phase information of the cross-spectrum, remained unchanged, i.e. 31.5% of the impeller rotation velocity.

So the identified unsteady pattern propagated not only inside the impeller, but also in the radial direction starting from the impeller discharge, preserving its pulsating characteristics and its rotating movement around the circumference.
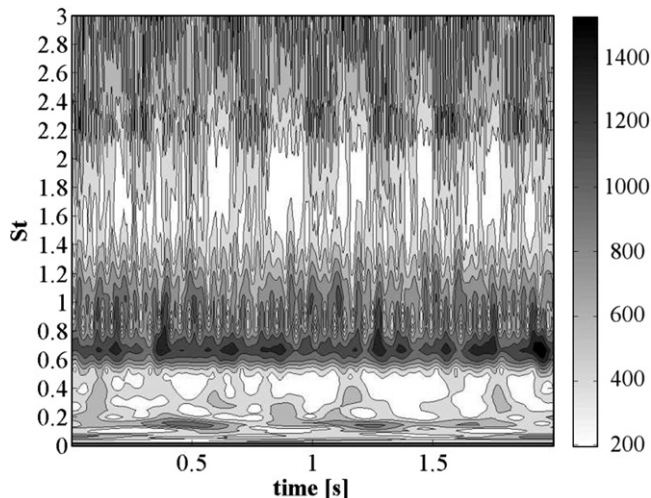

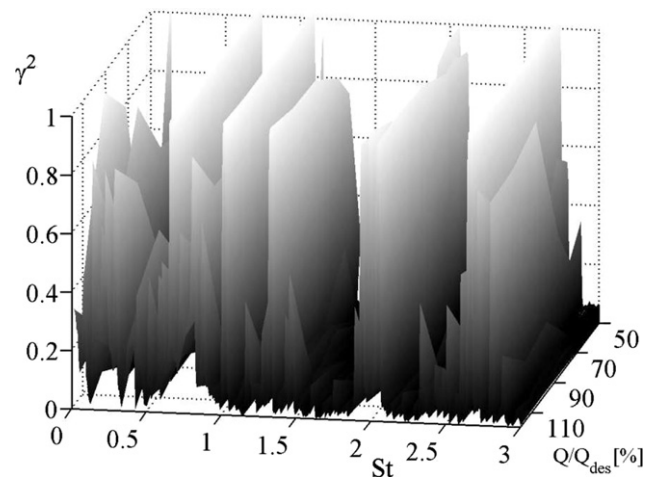Fig. 17. Wavelet transform magnitude |W| [Pa] in position 30 for Q/Q_{des} = 120% (n_i = 600 rpm).

Fig. 18. Coherence function between the pressure transducers in positions 30 and 31 (n_i = 600 rpm).

4.4. Pressure pulsations at a different impeller rotation speed ($n_i = 500$ rpm)

After analyzing of the influence of the radial distance on the un-steady pattern, the impeller rotation velocity was considered as second influencing factor. A second campaign of measurements was carried out at 500 rpm in order to compare the pressure sig-nals at different velocities.

Regarding the characteristic frequencies and the pulsating behaviour of the unsteady pattern, no significant changes were noted in any of the transducers throughout the working range. The unsteady pattern frequencies were still identifiable (Fig. 20), as well as their pulsation in time (Fig. 21 for $Q/Q_{des} = 80\%$).

As regards the rotation around the impeller discharge, the har-monics of the unsteady pattern as well as some non-linear interac-tion components, had greater values of both the cross-spectrum and the coherence function between the transducers placed at the same radial distance from the impeller discharge. Concerning this, Fig. 22 reports the coherence function between the transduc-ers in positions 30 and 31.

The propagation in the circumferential direction was confirmed in the time–frequency domains by the high levels of the cross-wavelet and of the wavelet coherence, that also highlighted a time-independent phase coincidence for the harmonics of the un-steady pattern throughout the range, as seen for $Q/Q_{des} = 120\%$ in Fig. 23.

Furthermore, the rotation velocity (31.5% of the impeller rota-tion velocity) was not modified by the different rotation velocity of the impeller.

To give explanation of its existence and its fluid-dynamical ori-gin, a hypothesis was formulated starting from the defined charac-teristics of the phenomenon. Two energy cores, having two different levels of energy, were supposed to pass around the impel-ler discharge, generating the pulsating behaviour of the structure, as seen by the time–frequency analysis throughout the working range.

This passage was time-independent and influenced the whole impeller discharge. The energy cores may be associated with the zones of jet and wake, localized at the impeller discharge and char-acterized by different energy levels. As these zones pass over the
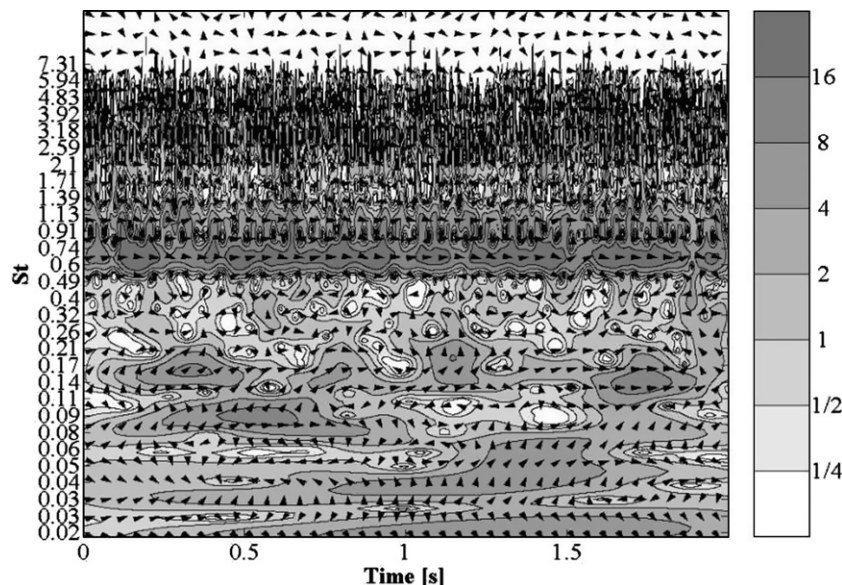

Fig. 19. Cross-wavelet transform between the pressure transducers in positions 30 and 31 for $Q/Q_{des} = 50\%$ ($n_i = 600$ rpm).
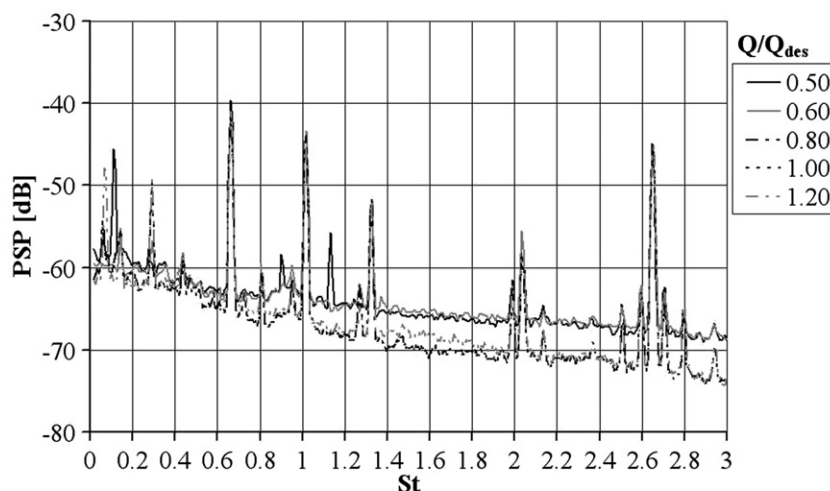

Fig. 20. Power spectrum [dB] of the pressure signal acquired in position 30 ($n_i = 500$ rpm).
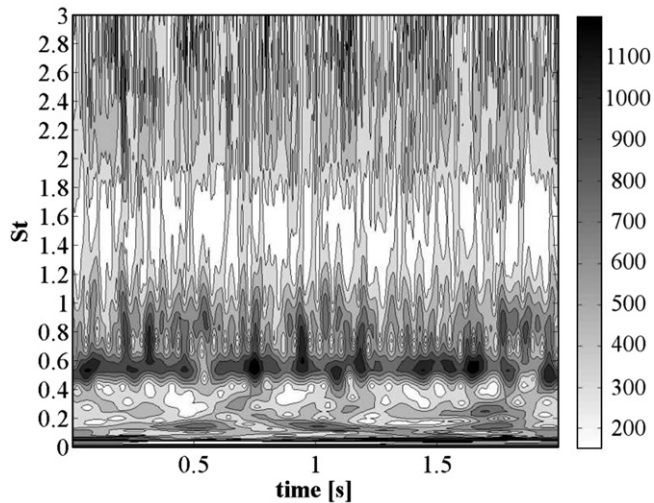
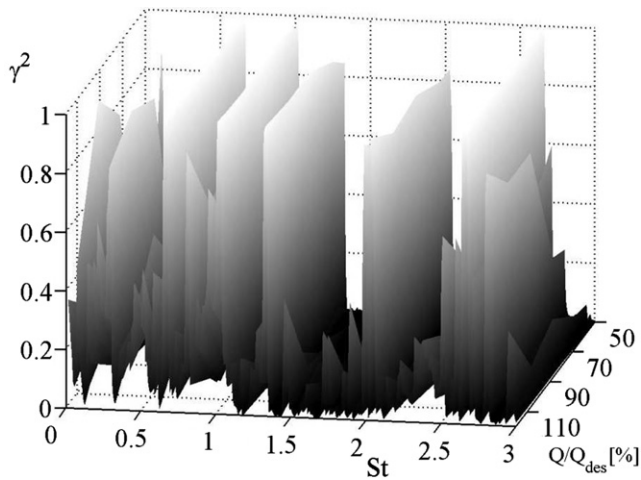**Fig. 21.** Wavelet transform magnitude $|W|$ [Pa] in position 30 for $Q/Q_{des} = 80\%$ ($n_i = 500$ rpm).

Fig. 22. Coherence function between the pressure transducers in positions 30 and 31 ($n_i = 500$ rpm).
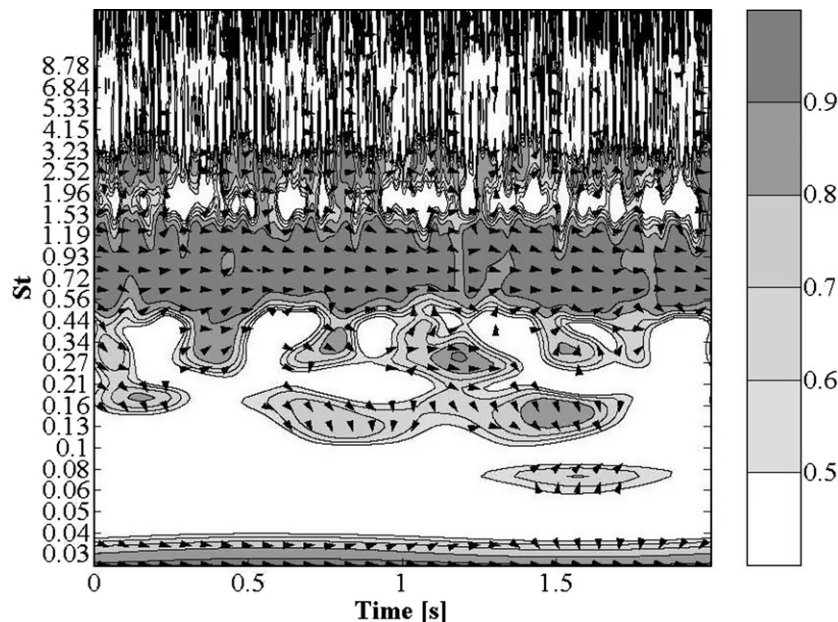
transducers, they could be perceived as pressure fluctuations, pulsating in time and rotating around the impeller discharge. This explanation was also in agreement with the greater amplitude of the peaks at low flow rates, as the jet-wake intensity decreased at the design and higher operating conditions. Therefore, characteristics of the identified structure allows for the assumption of a connection to the jet-wake phenomenon.

In Figs. 23 and 11 another frequency around $St = 0.14$ was characterized by significant values respectively of the coherence and of the cross-wavelet transform. This frequency disappeared at low flow rates (Fig. 16) and in the inlet duct (Fig. 9). These characteristics let suppose a connection of the frequency with a fluid-dynamical unsteadiness developing outside the measuring zone, probably in the elbow of the return channel. The absence of transducers placed in that zone prevented from giving further details of the evolution of the phenomenon in the return channel.

5. Conclusion

An experimental analysis was carried out on the flow field instability in an impeller, coupled with a vaneless diffuser to study the characteristics and the development of the unsteady phenomena. Acoustic measurements were acquired by means of pressure transducers, placed in the inlet duct and at the impeller discharge, at several angular and radial positions, for two different impeller rotation velocities, in order to identify the pulsating phenomena, define their characteristics and to evaluate their evolution in the radial direction and the influence of the impeller rotation velocity on their characteristics. The pressure signals were processed by the spectral analysis in the frequency and in the time–frequency domains to obtain information about the time evolution of the phenomena.

The analysis of the pressure signals highlighted the presence of a first pulsating phenomenon with a low frequency ($St = 0.071$), identified without the pump running, whose intensity increased with increasing flow rate. For these characteristics it was associated with the system fluctuations and in particular with the fluctuations of the water level in the accumulation tank of the pump. This hypothesis was strengthened by its greater intensity in the inlet duct.

Fig. 23. Wavelet coherence between the pressure transducers in positions 30 and 31 for $Q/Q_{des} = 120\%$ ($n_i = 500$ rpm).

On the other side, at the impeller discharge, a rotating structure of pressure pulsations was identified with the following characteristics:

- had a fundamental frequency at $St \simeq 0.664$ that was not associated with the blade passage frequency (BPF);
- interacted with both the blade passage frequency and with the system fluctuations, generating non-linear interaction components in the spectra;
- appeared and disappeared in time with regular intervals. The resulting structure was not frozen in time but it changed with a pulsating behaviour, depending on the constructive or destructive interference of its constituting modes;
- was present at all the operating conditions even tough its intensity was greater at low and high flow rates;
- rotated around the impeller discharge with a velocity of about 31.5% of the impeller rotation velocity;
- propagated to the impeller inlet and in the radial direction with the same characteristics;
- was not affected by the impeller rotation velocity.

This structure had a fluid-dynamical origin and it appears to be connected with the phenomenon, known as jet-wake.

The application of the frequency and time–frequency analysis was an indispensable tool in order to identify the structure and all its characteristics.

Acknowledgement

References

Akin, O., Rockwell, D.O., 1994. Actively controlled radial flow pumping system: manipulation of spectral content of wakes and wake-blade interactions. J. Fluids Eng. 116, 528–537.

Ardizzon, G., Pavesi, G., 2004. Analysis of unsteady flow in a vaned. In: Bohn, Dieter (Ed.), The 10th Intl Symp. on Transport Phenomena and Dynamics of Rotating Machinery, vol. 218. The Pacific Center of Thermal-Fluids Engineering, pp. 23–51.

Bent, P., 1993. Experiments on the aerodynamic generation of noise in centrifugal turbomachinery. PhD Thesis, The Pennsylvania State University, University Park.

Choi, J.-S., 1991. Experiment on the unsteady flowfield associated with the noise generation in a centrifugal turbomachinery. PhD Thesis, The Pennsylvania State University, University Park.

Choi, J.-S., McLaughlin, D.K., Thompson, D.E., 2003. Experiments on the unsteady flowfield and noise generation in a centrifugal pump impeller. J. Sound Vib. 263, 493–514.

Cumpsty, N.A., 1977. Review – a critical review of turbomachinery noise. J. Fluids Eng. 99, 278–293.

Embleton, T.F.W., 1963. Experimental study of noise reduction in centrifugal blower. J. Acoust. Soc. Am. 35, 700–705.

Farge, M., 1992. Wavelet transforms and their application to turbulence. Annu. Rev. Fluid Mech. 24, 395–457.

Ferrara, G., Ferrari, L., Baldassarre, L., 2004. Rotating stall in centrifugal compressor vaneless diffuser: experimental analysis of geometrical parameters influence on phenomenon evolution. Int. J. Rotating Mach. 10 (6), 433–442.

Horodko, L., 2006. Identification of rotating pressure waves in a centrifugal compressor diffuser by means of the wavelet cross-correlation. Int. J. Wavelets, Multiresolution Inf. Process. 4 (2), 373–382.

Horodko, L., 2007. Detection of surge precursors in a centrifugal compressor with a wavelet method. In: Papailiou, K.D., Martelli, F., Manna, M. (Eds.), The Seventh European Turbomachinery Conference National Technical University of Athens, pp. 317–326.

Koopmann, G.H., Fox, D.J., Neise, W., 1988. Active source cancellation of blade tone fundamental and harmonics in centrifugal fans. J. Sound Vib. 126 (2), 209–220.

Li, H., 1998. Identification of coherent structure in turbulent shear flow with wavelet correlation analysis. J. Fluids Eng. 120, 778–785.

Mongeau, L.G., 1991. Experimental study of the sound generation by rotating stall in centrifugal turbomachines. PhD Thesis, The Pennsylvania State University, University Park.

Mongeau, L.G., Thompson, D.E., McLaughlin, D.K., 1993. Sound generation by rotating stall in centrifugal turbomachines. J. Sound Vib. 163 (1), 1–30.

Neise, W., 1976. Noise reduction in centrifugal fans: a literature survey. J. Sound Vib. 45 (3), 375–403.

Neise, W., Koopmann, G.H., 1980. Reduction of centrifugal fan noise by use of resonators. J. Sound Vib. 73 (2), 297–308.

Torrence, C., Compo, G., 1998. A practical guide to wavelet analysis. Bull. Am. Meteorol. Soc. 79 (1), 61–78.

Torrence, C., Webster, P.J., 1999. Interdecadal changes in the enso-monsoon system. J. Climate 12, 2679–2690.